Temperature Decoupling of a Hydrogel-Based Strain Sensor under a Dynamic Temperature Field

Zemin Li, Jiaoya Huang, Runhui Zhou, Ziyu Chen, Wenchao Gao, Jiang He,* Rongrong Bao,* and Caofeng Pan**

Hydrogels possess several interesting characteristics and have attracted increasing attention for flexible interactive strain-sensing. However, hydrogel strain sensors are easily influenced by temperature because of the intrinsic characteristics of the materials, thus, their sensing accuracy is significantly affected. Herein, a strategy is proposed to eliminate the influence of temperature by building an in-situ hydrogel temperature sensor next to the strain sensor to monitor ambient temperature changes and simultaneously correct the strain signal. By introducing silicon nanoparticles and modified graphene, the hydrogel exhibits a good balance between conductivity and stretchability. The hydrogel strain sensor exhibits a working range of up to 1000% and a sensitivity of 8.1. It can monitor human movement and shows good stability. Moreover, the hydrogel-based sensor demonstrates an impressive thermal response sensitivity (−7.16% °C^{-1}). This bimodal sensor not only realizes the decoupling of the strain sensor from the temperature but protects the temperature sensor from the influence of strain. More importantly, the device is also able to accurately control the manipulator under dynamic temperatures, proving the feasibility of the design. This strategy provides a new method to eliminate the influence of temperature on strain sensing and assists in the development of the interactive-sensing field.

1. Introduction

With the development of intelligent technology, sensing devices have progressed significantly,[1] and contactless human–machine interactive sensing and noninvasive health monitoring have been widely used in daily life,[2] especially during the current pandemic. Flexible sensors, which could convert physical or chemical signals into recordable electrical signals, are an indispensable part of electronic integration systems for detecting external stimulation, which has good conformability.[3] Human skin is an excellent multifunctional sensor that can sense a wide variety of external stimulation, including strain, pressure, and temperature. Therefore, many kinds of skin-like sensors have been developed rapidly.[3a,4] Among them, strain sensors are favored by researchers because of their simple fabrication and wide application, including noninvasion healthcare and human–machine interaction. Flexible strain sensors have been upgraded and optimized from materials to structures to accurately perceive external stimuli. The patterned structure is a commonly used method to enhance the sensitivity and broaden the response range of strain sensors. Patterned structures,[5] such as pyramidal, porous, serpentine, and Kirigami structures, improve the sensing accuracy and sensing range of the sensor. Another method is combining flexible materials,[6] such as polydimethysiloxane (PDMS), hydrogels, styrene ethylene butylene styrene (SEBS), and thermoplastic polyurethane (TPU). Flexible materials can meet various needs

---

Z. Li, R. Bao
School of Chemistry and Chemical Engineering
Guangxi University
Nanning, Guangxi 530004, P. R. China
E-mail: baorongrong@binn.cas.cn

Z. Li, J. Huang, R. Zhou, Z. Chen, W. Gao, J. He, R. Bao, C. Pan
CAS Center for Excellence in Nanoscience
Beijing Key Laboratory of Micro-nano Energy and Sensor
Beijing Institute of Nanoenergy and Nanosystems
Chinese Academy of Sciences
Beijing 101400, P. R. China
E-mail: gaowenchao@binn.cas.cn; hejiang@binn.cas.cn; cfpan@binn.cas.cn

J. Huang, Z. Chen, C. Pan
Center on Nanoenergy Research
School of Physical Science and Technology Guangxi University
Nanning, Guangxi 530004, P. R. China

R. Zhou, R. Bao, C. Pan
School of Nanoscience and Technology
University of Chinese Academy of Sciences
Beijing 100049, P. R. China

The ORCID identification number(s) for the author(s) of this article can be found under https://doi.org/10.1002/admt.202300404

DOI: 10.1002/admt.202300404

of flexible strain sensors. They can be used as sensing layer by doping conductive fillers, or directly used as stretchable layers and adhesive layers without complex structure and processing.

Compared with traditional rigid materials, flexible materials that have good conformability, can greatly improve the accuracy of strain-sensing signals, and enhance the comfort of wearing. As typical flexible material, hydrogels have many interesting characteristics (compliance, stretchability, conductivity, printability, biocompatibility, etc.) and have facile processing, making them promising candidates for soft sensing.[7] Hydrogel can be used as a sensing active material because of its good conductivity. Generally, there are two ways to make hydrogels conductive: one is to choose the inherently conductive polymer (polyaniline (PANI), poly(3,4-ethylenedioxythiophene)-poly(styrenesulfonate) (PEDOT:PSS), polypyrrole (PPy)) as the main network of the hydrogel,[7b,8] and the other is to dope conductive fillers (graphene, MXene, metal nanowires, carbon nanotubes, liquid metals (LMs), and ionic liquids).[7c,9] However, the higher the proportion of conductive components is, the worse the tensile property of hydrogel will be.[10] More importantly, the hydrogel is very sensitive to temperature due to the intrinsic characteristics of the sensing material, making the sensor easily affected by temperature. The complex thermal effect would have an adverse impact on the practical application of interactive sensing due to the unstable working environment.[11] Generally, temperature decoupling can be usually realized by using a built-in circuit or numerical calibration.[12] However, the current work on temperature decoupling involved a complex calculation process. Therefore, it is urgent to explore a simple and universal strategy to realize the temperature decoupling of the hydrogel strain sensor.

Here, we propose a general strategy to eliminate the influence of temperature on strain sensing, that is, the strain sensor is connected in series with the temperature sensor. Then, the real deformation signal of the strain sensor in the variable temperature environment can be obtained through a simple calculation based on the relationship between the temperature and conductivity of the hydrogel. First, to balance the mechanical and electrical properties of the hydrogel, we introduced long-chain silicon nanoparticles to replace the traditional cross-linking agent, and conductive graphene and PEDOT:PSS were modified by hydrophilic dopamine, enhancing the binding force between the hydrogel body and the conductive components. The hydrogel not only possessed a fracture strain of over 5000% and a conductivity of 10 S m^{-1} but also had printability and self-healing capability. The hydrogel-based sensor exhibited excellent strain-sensing performance, with the sensitivity reaching 8.1 at 1000% strain, while also being sensitive to temperature. The strain sensor showed more than 10 000 cycles of stability at 100% strain. Notably, the strain sensor detected human motions, including changes in facial expressions. The hydrogel-based sensor exhibited a high sensitivity of −7.16% °C^{-1} over a sensing range of 7–20 °C, and the maximum detectable temperature reached 60 °C. A bimodal sensor based on a parallel connection of the temperature and strain sensors realized the temperature decoupling of strain through a simple calculation, obtaining the real deformation value under a dynamic temperature field, and the temperature sensor was not affected by strain. Notably, this device realized precise control of a manipulator in a stochastic environment. This strategy provides a new approach for the accurate operation of strain sensors in complex temperature environments.

2. Results and Discussion

2.1. Synthesis and Characterization of the Hydrogel

To balance the stretchability and conductivity of the hydrogel, long-chain silicon nanoparticles (LSNPs) were synthesized using the sol–gel method, with modified γ-methacryloxypropyl trimethoxy silane (KH-570) replacing the traditional cross-linker, as shown in Figure S1 (Supporting Information).[13] By adjusting the proportions of polyvinyl alcohol (PVA), acrylamide monomer, and LSNPs, we obtained an optimal ultrastretchable hydrogel ratio (Figure S2, Supporting Information). Graphene has excellent electrical conductivity; however, its intrinsic characteristic of hydrophobicity limits its uniform dispersion in hydrogels, thus reducing the conductivity of the hydrogel. With dopamine having a dynamically balanced molecule structure (the quinone and catechol groups), it can form hydrogen bonds and π–π conjugates with other materials, which can assist in the dispersion of other hydrophobic molecules.[14] Thus, dopamine and PEDOT:PSS were used to modify graphene to enhance its hydrophilicity and conductivity to obtain conductive nanosheets (Figure S3, Supporting Information).[15] It can be seen from the optical images that dopamine-modified graphene and PEDOT:PSS (PDGP) has better dispersion than graphene (Figure S4, Supporting Information). Raman spectra were obtained to further demonstrate the successful synthesis of the PDGP conductive nanosheets (**Figure 1**c). The characteristic peaks of graphene at 1350 cm^{-1} (D peak) and 1591 cm^{-1} (G peak) and the $C_\alpha = C_\beta$ symmetric stretching at 1430 cm^{-1} of PEDOT occurred simultaneously, which implied the formation of conductive nanosheets. Figure 1a shows the detailed preparation of the hydrogel, which consisted of three types of networks: conductive, stretchable, and self-healing. The conductive nanosheets reinforced the electromechanical properties of the hydrogel. Additionally, the hydrogel possessed excellent printability, allowing elaborate pattern fabrication (Figure S5, Supporting Information). Scanning electron microscopy (SEM) of the lyophilized conductive hydrogel shows the presence of conductive nanosheets (Figure 1b). Fourier transform infrared (FTIR) spectra were obtained to confirm the formation of chemical bonds within the conductive hydrogel (Figure 1d). The absorption peak of the –OH groups at 3294 cm^{-1} for PVA and polydopamine (PDA) shifted to 3203 cm^{-1}, and the peaks of the –NH groups at 3338/1609 cm^{-1} for polyacrylamide (PAM) shifted to 3320/1600 cm^{-1}, indicating the formation of hydrogen bondings between them. The electromechanical performance of the $P_{0.45}P_1$–G_mP_n hydrogels (simplified as G_mP_n hydrogel in figure, the first P stands for PVA, the second P for PAM, the third P for PEDOT:PSS, G for graphene; m and n representing the mass concentrations of graphene and PEDOT:PSS in hydrogels, respectively) was investigated as follows. The mechanical properties of the conductive hydrogels were evaluated using tensile stress–strain measurements. The hydrogel could be stretched to more than 50 times its original length, which helped to avoid fracture failure under large deformations, and the mechanical properties can be restored to 80% after self-healing (Figure 1e). A cuboid $P_{0.45}P_1$–$G_{0.4}P_1$ hydrogel was prepared ($1.5 \times 1.5 \times 1.5$ cm^3)

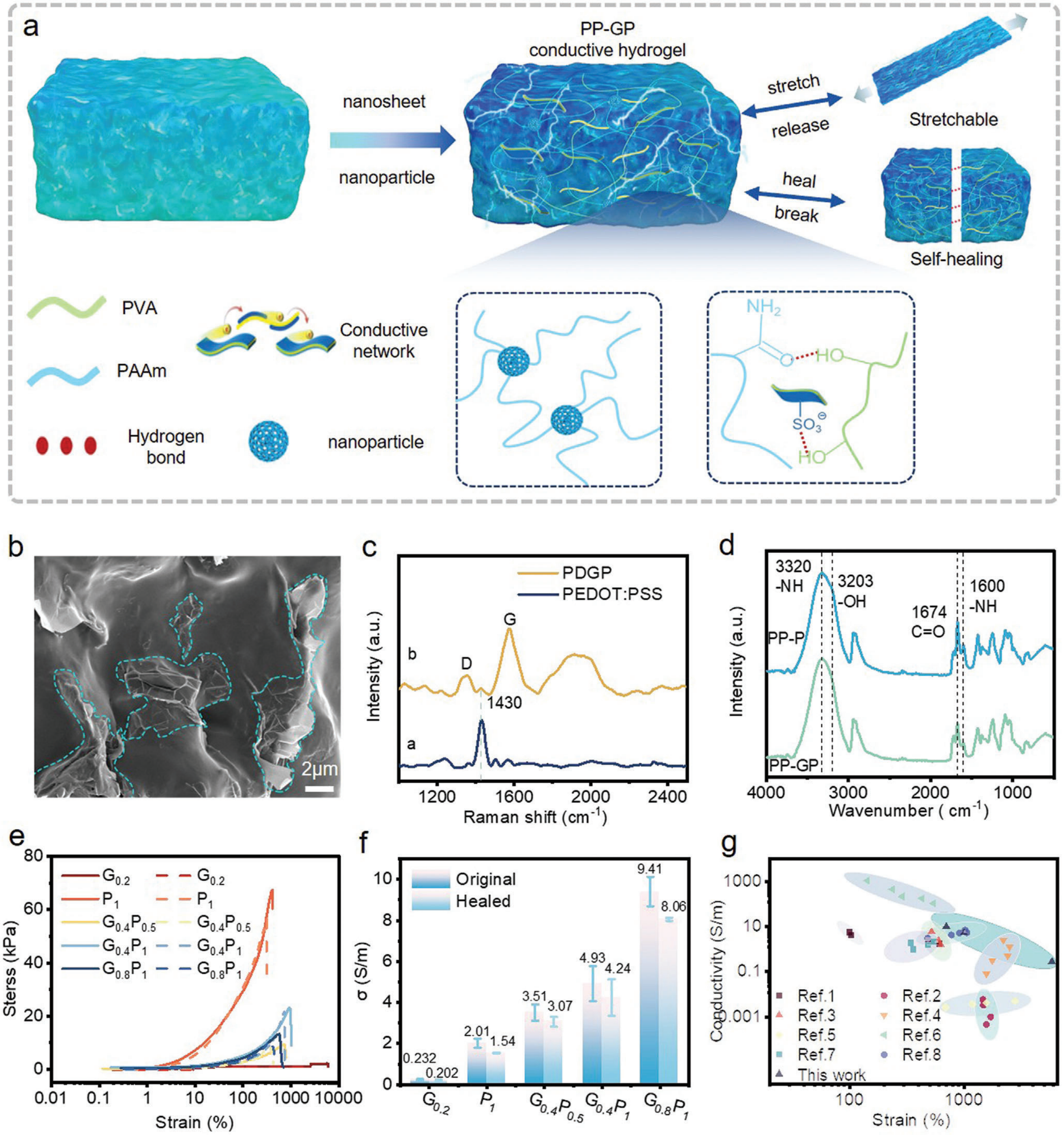

Figure 1. Design principle and material characteristics. a) Schematic of the synthetic route of the conductive hydrogel. b) SEM images of the conductive hydrogel (the areas circled by the blue dotted line are the nanosheets). c) Raman spectra of PDGP and PEDOT:PSS nanosheets. d) FTIR spectra of the PP–GP and PP–P hydrogels. e) Stress–strain curves and f) conductivity of the $P_{0.45}P_1$–G_mP_n hydrogels before and after self-healing. g) Comparisons of the maximum tensile strain and conductivity with recently reported printable conductive hydrogels.

to measure the conductivity of the hydrogel using the two-probe method on an electrochemical system. It is evident that the conductivity of the hydrogel increased with increasing concentration of the conductive filler (Figure 1f). The $P_{0.45}P_1$–$G_{0.8}P_1$ hydrogel exhibited better conductivity (reaching 10 S m^{-1}) than the graphene and the PEDOT:PSS hydrogels, which was attributed to PDA accelerating the homogeneous dispersion of the nanosheets. To demonstrate the comprehensive performance of the hydrogel, it was connected to a circuit (working voltage of 5 V), and its performance was macroscopically displayed by

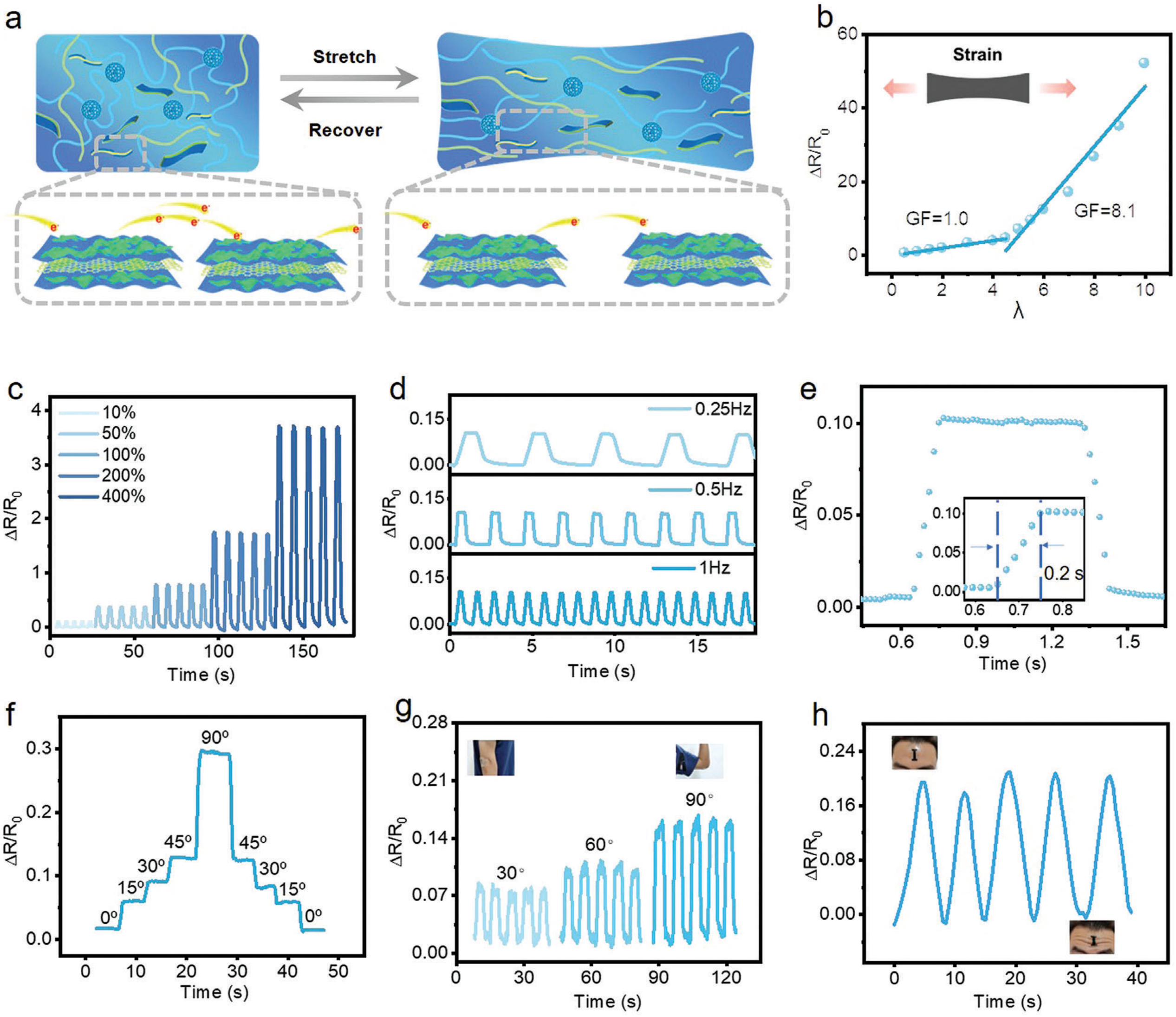

Figure 2. Strain-sensing performance of the hydrogel-based sensor. a) Strain sensing mechanism and b) relative resistance variation of the at different strains of the hydrogel-based sensor. Response curves of the strain sensor with c) an applied stepwise strain and d) the different frequencies at 10% strain. e) Response time curve of the strain sensor with an applied 10% strain. Demonstration of strain sensors for human body monitoring, such as f) finger, g) elbow, and h) the forehead.

observing changes in the light-emitting diodes (LEDs) (Figure S6, Supporting Information). The LEDs darkened after stretching because of the reduced cross-sectional area of the hydrogel, which led to an increase in resistance. Once the conductive hydrogel was cut entirely, the circuit broke and the LEDs were no longer lit. However, by contacting the ruptured hydrogel, the dynamic hydrogen bonds inside the hydrogel were re-established, allowing it to heal, resulting in a complete circuit, and the LEDs became lit again. The distinct advantages of the $P_{0.45}P_1$–$G_{0.8}P_1$ hydrogel over most hydrogels reported thus far in electronic sensor applications are shown in Figure 1g (details in Table S1 in the Supporting Information). The high conductivity, stretchability, printability, and self-healing ability of the $P_{0.45}P_1$–$G_{0.8}P_1$ hydrogel demonstrates its feasibility for use in stretchable electronic skins and flexible wearable devices.

2.2. Effect of Strain on the Hydrogel-Based Sensor

The addition of the conductive nanosheets improved the strain response of the hydrogel. As shown in **Figure 2**a, the distance between the adjacent nanosheets increased after stretching the hydrogel; therefore, the number of mobile electrons decreased and the resistance of the hydrogel increased. The relative resistance variation ($\Delta R/R_0$) of the hydrogel-based sensor at different strains was investigated (Figure 2b). The $\Delta R/R_0$ value increased monotonously with an increase in the tensile strain throughout the entire stretching process. When the tensile strain range was less than 450%, the gauge factor (GF) was 1.0, but it changed to 8.1 in the range of 450–1000%, presenting a nonlinear response. Figure 2c shows the cyclic response of the hydrogel sensor to stepwise strains (from 10% to 400%); the relative

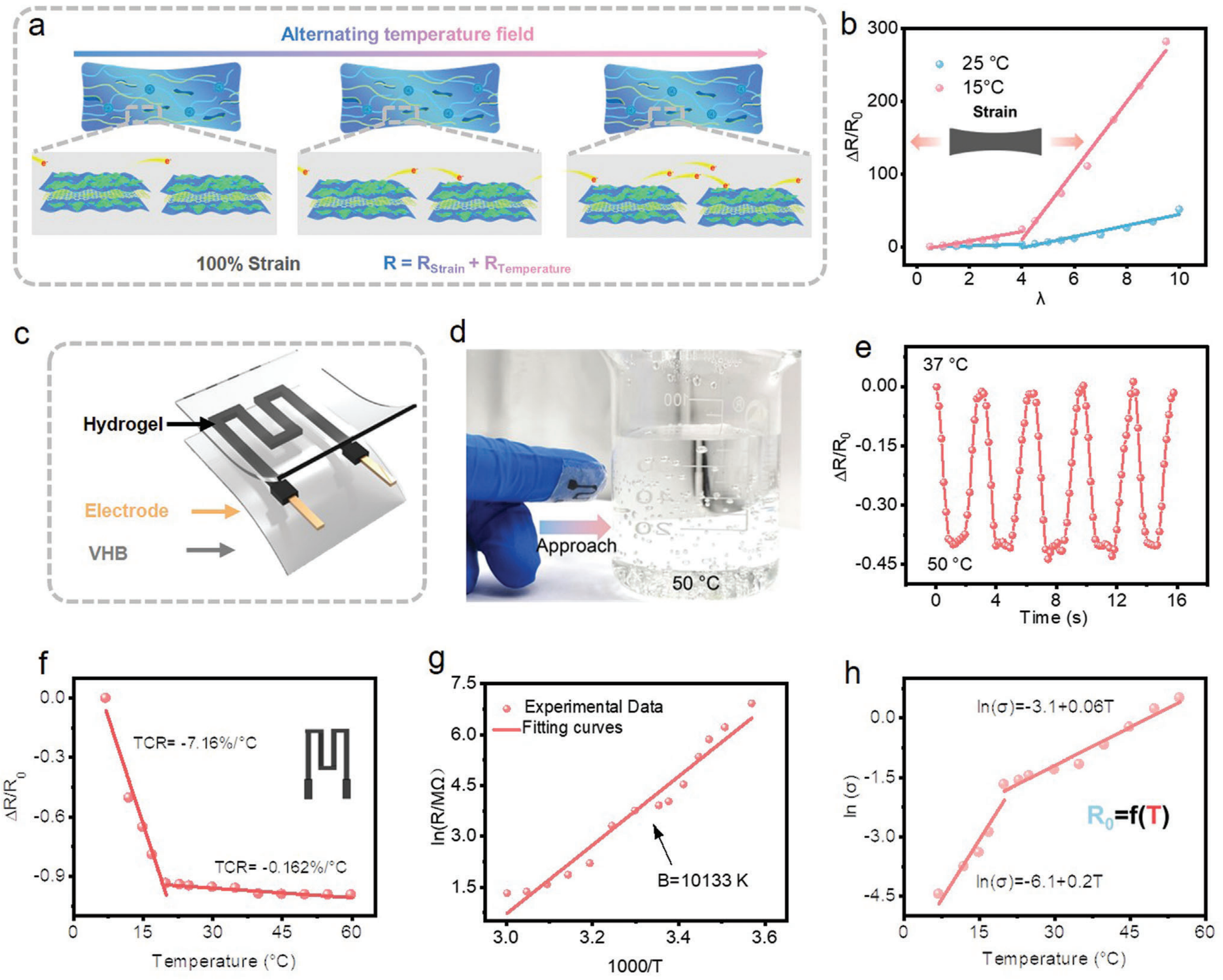

Figure 3. Effect of temperature on hydrogel-based sensor. a) Effect of temperature on the hydrogel-based sensor at 100% strain. b) Response curve of the hydrogel-based sensor at two temperatures. c) The explosion diagram of the hydrogel-based temperature sensor. d) Picture and e) relative resistance change of temperature sensor attached to the finger near and departed away from hot water (50 °C). f) Normalization relative resistance changes of encapsulated hydrogel upon increasing temperature from 7 to 60 °C. g) Arrhenius plot shows linear dependence of ln(*R*) on 1000/*T*. h) The various conductivities with the temperature for the hydrogel-based sensor.

resistance variation increased with the strain, and the sensor could output a steady signal. Similarly, the responses at different frequencies (0.25, 0.5, and 1 Hz) under 10% strain are exhibited in Figure 2d, indicating that the hydrogel-based sensor can be applied to various strain-induced scenarios. In addition, the response time to the applied strain was recorded, and the time was only 0.2 s under 10% strain at 0.5 Hz (Figure 2e). Based on the excellent strain-sensing performance of the hydrogel sensor, it was used to monitor human body movement. The strain sensor was subjected to over 10 000 stretching and releasing cycles between 0% and 100% strain at a strain rate of 0.8 mm s^{-1}, demonstrating reliable cyclic stability and duration (Figure S7, Supporting Information). As shown in Figure 2f–h, the strain sensor could accurately distinguish the angle of finger and elbow bends and recognize forehead expressions, which demonstrates the potential application of the sensor in healthcare and human–machine interactions. The above tests demonstrate that the strain sensor can monitor both small and large deformations of the human body in complex external environments.

2.3. Effect of Temperature on the Hydrogel-Based Sensor

The electron mobility of the conductive hydrogel varied with temperature at the same strain because of the intrinsic characteristics of the conductive material; therefore, the resistance of the hydrogel sensor changed with temperature (**Figure 3**a). The resistance of graphene and PEDOT:PSS will gradually decrease with the increase of temperature, so the sensor using them as sensing material exhibits a negative temperature coefficient.[2a,16] The single-mode strain sensor has been stretched for a certain number of times at five temperatures, respectively. As shown in Figure S8

(Supporting Information), it can be seen that the response of the single-mode strain sensor to 100% strain varies with temperature. As the temperature increases, the value of $\Delta R/R_0$ decreases, and the relative resistance change value at this time is composed of temperature signal and deformation signal. As shown in Figure 3b, the response of the hydrogel-based sensor to the same deformation was different at the two temperatures, which was unfavorable for strain sensors in practical scenarios. Hence, a strategy to eliminate the influence of temperature was proposed, which was to construct a temperature sensor beside the strain sensor to monitor environmental changes and then obtain the real deformation value based on a simple calculation. Similar to the strain sensor, the temperature sensor was printed using a microelectronic printer with the same hydrogel material (Figure 3c). First, the sensor perceptibility was investigated at variational temperatures. Figure 3d,e shows the photograph and actual electrical signal of the temperature sensor attached to a finger near a cup of 50 °C water. The temperature sensor quickly and steadily responded to environmental changes, demonstrating its excellent temperature-sensing ability. As shown in Figure 3f, the $\Delta R/R_0$ valve of the temperature sensor decreased as the temperature increased, showing a negative temperature response, which can be attributed to the increase of the electron transmission between conductive nanosheets with the rise of temperature. The temperature coefficient of resistance (TCR) as an evaluation criterion for the thermal sensitivity of temperature sensors was quantified as follows

$$\mathrm{TCR} = \frac{1}{R_0} \cdot \frac{\Delta R}{\Delta T} \tag{1}$$

where R_0 was the initial resistance of the temperature sensor at 7 °C, and ΔR was the resistance change corresponding to temperature change ΔT. The obtained TCR value was -7.16% °C^{-1} at 7–20 °C and -0.162% °C^{-1} at 20–60 °C, which surpassed those of most reported temperature sensors. The resistance change was obvious in the temperature range from 7 to 60 °C. Therefore, we constructed a fitting curve of $\ln(R)$ versus $1/T$ using the Arrhenius law as follows

$$\ln(R) = \ln(R_0) + \frac{B}{T} \tag{2}$$

The slope of the fitted curve corresponding to the material constant of thermistor B was 10 133 K, indicating the excellent temperature sensitivity of the hydrogel-based sensor. The conductivity of the hydrogel changes with temperature because of its intrinsic characteristics; therefore, the strain sensor has different initial resistance values at different temperatures. The following equation was obtained by fitting the relationship between the conductivity and temperature (Figure 3h)

$$\ln(\delta) = -6.1 + 0.2T \tag{3}$$

$$\ln(\delta) = -3.1 + 0.06T \tag{4}$$

where δ was the conductivity of the hydrogel. Hence, we can obtain the initial resistance at any temperature based on the relationship between the resistance and conductivity, thus decoupling the strain from the temperature.

2.4. Strain and Temperature Bimodal Sensor and Strain Calibration in a Dynamic Temperature Field

A bimodal sensor was designed by connecting the strain and temperature sensors in series to counteract the effect of temperature on the strain (**Figure 4**a). To eliminate the effect of strain on the temperature sensing unit, hard-film polyethylene terephthalate (PET) was placed under the temperature sensor acting as a strain-inhibiting layer, the protective mechanism of which is illustrated in Figure 4b. The bimodal sensor contained two regions. When the strain-sensing region was subjected to large deformation, the temperature-sensing region showed insignificant change due to the protection of rigid PET. As shown in Figure 4c, the stiff region (temperature-sensing region) was hardly deformed when the bimodal sensor was stretched. The mechanical simulation results further proved that the PET protected the temperature sensor from strain (Figure S9, Supporting Information). By measuring the dynamic response curves of the temperature sensor during heating and cooling under different strains, it was found that the response of the temperature sensor to the temperature change (from 20 to 43 °C, down to 20 °C and then up to 50 °C) was the same when the strain was applied and not applied, indicating the strain insensitivity of the temperature-sensing unit (Figure 4d). The true deformation signal was then obtained using the relationship between the conductivity of the hydrogel and temperature. Figure 4e shows the calibration of the 15 °C strain response curve, where the response curve at 15 °C was consistent with that at 25 °C, that is, the true deformation value was obtained. The calibrated strain signal exhibited good stability (Figure 4f). The device was designed to control a manipulator in a dynamic temperature field to demonstrate the practicability of this strategy. Then, based on Figure S10a (Supporting Information) circuit control system, the single-mode strain sensor was used to control the movement of the manipulator. It could be seen from Figure S10b (Supporting Information) and Movie S1 (Supporting Information) that at room temperature, the single-mode strain sensor can perform a stable interaction process. However, when the ambient temperature gradually increases, the deformation signal is mixed with temperature noise, which causes the incorrect movement of the manipulator. Therefore, after the temperature rises, even if the finger does not deform, the manipulator would go from a bent state to a straight state (Figure S10b$_3$, Supporting Information). The bimodal sensor controls the manipulator based on the control circuit shown in Figure 4g. Due to temperature compensation, the movement of the manipulator can be accurately controlled by the bimodal sensor in the dynamic temperature field without temperature interference (Figure 4h$_3$,h$_4$ and Movie S2 (Supporting Information)).

3. Conclusion

In summary, this study employed a flexible printing technology to construct a temperature sensor next to a strain sensor, offsetting the influence of temperature on strain sensing. First, the

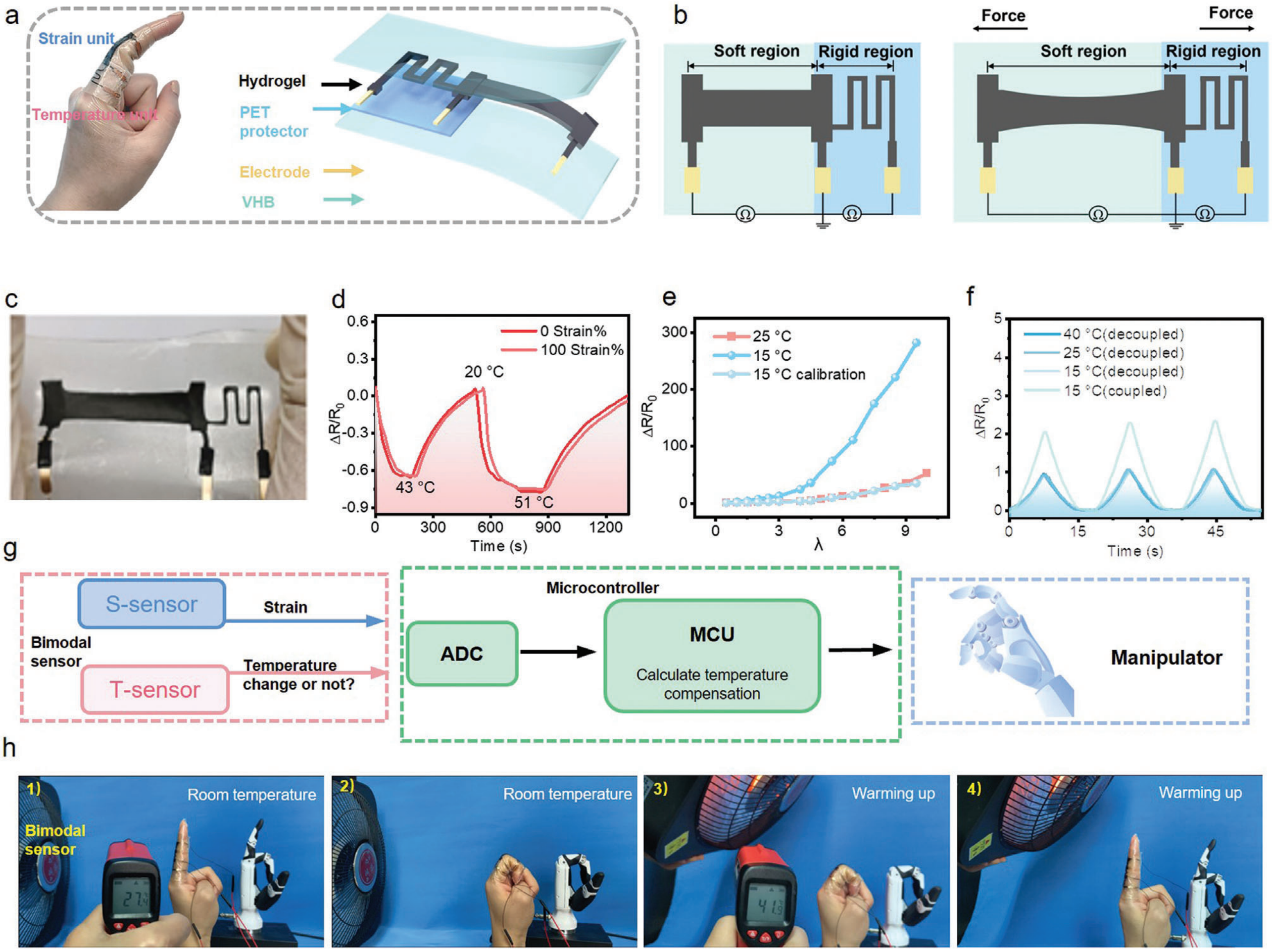

Figure 4. Decoupling of temperature by strain sensor. a) Schematic diagram of the hydrogel-based bimodal sensor. b) Schematic and c) picture of PET protecting the temperature sensing unit of the devices from strain. d) Temperature response curves of the device at different strains, indicating the strain insensitivity of the temperature sensing unit during temperature sensing. e) The response of the strain sensing part after calibration at 15 °C. f) Cycle response of the strain sensing unit before and after decoupling. g) Flowchart of bimodal sensor controlling the manipulator at dynamic temperature field. h) Optical picture of bimodal sensor controlling the manipulator under stochastic environment.

temperature-sensitive conductive nanosheet was synthesized utilizing graphene, PEDOT:PSS, and hydrophilic dopamine. Then, a conductive triple-network hydrogel was achieved by doping the nanosheets into the PVA–PAM double network, and the optimal proportions of polymers, LSNPs, and nanosheets were investigated based on the mechanical and conductive properties of the hydrogel. The single-mode hydrogel sensor possesses prominent sensing ability for strain and temperature, in which the GF of strain sensing reaches 8.1 under 1000% strain and the thermal index of the temperature sensor unit can reach 10 133 K between 7 and 60 °C. To eliminate the impact of temperature on strain sensing, a temperature sensor was fabricated next to the strain sensor, and the real deformation was obtained based on a simple calculation at any temperature. The structural design allowed the response of the temperature sensor to be free from strain. The accurate transmission of finger deformation signals to the manipulator in real time at various temperatures demonstrates the feasibility of this strategy.

4. Experimental Section

Materials: All chemical reagents were used in this work without further purification. PVA (average polymerization degree = 2400 ± 50, Shanghai Yingjia Co., Ltd.), PEDOT:PSS particles (Soochow Liyan Materials Co., Ltd.), acrylamide (AAm, 99%, Aladdin), dopamine hydrochloride (Aladdin), ammonium persulfate (APS, Aladdin), *N*,*N*-methylenebisacrylamide (99%, Aladdin), *N*,*N*,*N′*,*N′*- tetramethylethylenediamine (TMEDA, 99%, Aladdin), Fs-300 (Nuochen International Trading Co., Ltd.), ammonium hydroxide ($NH_3 \cdot H_2O$, AR, 99%, Macklin), *γ*-methacryloxypropyl trimethoxy silane (KH-570, Beijing Chemical Reagent Company, China). Graphene was prepared according to the previously reported method,[17] VHB (400 µm, VHB4920, 3M). Deionized water was obtained in the laboratory.

Preparation of Ultrastretchable P_xP_1 Hydrogels: Ultrastretchable P_xP_1 hydrogels were synthesized using a simple one-pot method. LSNPs were synthesized according to a previously reported method, in which 0.83 g of KH-570 was added into 10 g of deionize (DI) water, and the mixture was vigorously stirred for 24 h at room temperature. After the oil-like droplets disappeared, an emulsion of LSNPs was obtained. The emulsion (1 mL) was diluted with DI water to a final volume of 10 mL. PVA powder was then placed in DI water with magnetic stirring at 90 °C for 9 h. Therefore, AAm powder, Fs-300, glycerin, APS, and TMEDA were added to aqueous PVA, followed by stirring to achieve uniform dispersion, and the solution was later dropped into a polytetrafluoroethylene (PTFE) mold heated at 60 °C for 15 min to obtain the ultrastretchable P_xP_1 hydrogels.

Preparation of PDGP: 0.32 g dopamine powder and 0.4 g graphene were dissolved in water with stirring for several minutes at room temperature. Afterward, the $NH_3 \cdot H_2O$ was added to the above solution by stirring for 30 min at 5 °C, then stirring for 12 h at 40 °C to obtain PDA–G dispersion. Then, a series of PEDOT:PSS was put into the PDA–G dispersion by stirring for 12 h at 40 °C, obtaining the PDGP.

Preparation of P_xP_1–G_mP_n Hydrogels: For preparing P_xP_1–G_mP_n hydrogels, AAm powder, Fs-300, glycerin, PDGP, APS, and TMEDA were added to the PVA aqueous solution, followed by uniform dispersion. Subsequently, the conductive hydrogel precursor obtained was dropped into a PTFE mold heated at 80 °C for 15 min to obtain the flexible conductive P_xP_1–G_mP_n hydrogels. The precursor was transferred to a syringe for direct ink writing.

Characterization: Lyophilizer (Christ ALPHA 1-2LDplus) was used for dried the sample. The morphology of $P_{0.45}P_1$–$G_{0.8}P_1$ hydrogel was characterized by SEM and LSNPs were characterized by transmission electron microscope (TEM). FTIR and Raman spectra were obtained using Fourier transform infrared spectrometer (Bruker VERTEX80v) and Confocal micro-Raman spectrometer (HORIBA JY, LABRAM HR EVOLUTION), respectively. The mechanical properties were tested by a tensile machine (Yuelian YL-S71). The conductivity of the hydrogels was measured using a two-probe method on an electrochemical system (Metrohm PGSTAT302N, Switzerland) according to a previously reported procedure. A flexible electronics printer performed the customized hydrogel structure (Module Columbus, Shanghai, China). The electrical signals of strain and temperature sensing were collected and recorded by an LCR meter (Agilent E4980A). A linear motor (LinMot1100) was used to offer mechanical motions.

Finite Element Simulation for the Strain Isolation Effect of PET: The bimodal sensor's stress distribution and real-time state were simulated by using commercial software Abaqus (version 2020). The thickness of the hydrogel was 374 µm, and Young's modulus of hydrogel was 32.5 kPa. The dimension of VHB was 60 mm (length) × 40 mm (width) × 0.5 mm (thickness), and Young's modulus was 50 kPa. The dimension of PET was 50 mm (length) × 35 mm (width) × 0.05 mm (thickness), the strength was 60 kPa, and Young's modulus was 3000 MPa. To analyze the mechanical behavior of these elastomers, one side of the bimodal sensor was fixed and 100% strain was applied to the other side.

Supporting Information

Supporting Information is available from the Wiley Online Library or from the author.

Acknowledgements

The authors are grateful to Junyuan Tian for his help with the preparation of figures in this paper. The authors thank the support of the National Natural Science Foundation of China (Grant Nos. 52003101, 52125205, U20A20166, 61805015, and 61804011), the Natural Science Foundation of Beijing Municipality (Grant No. Z180011), the China Postdoctoral Science Foundation (Grant Nos. 2020M673052, 2021T140270), the Shenzhen Science and Technology Program (Grant No. KQTD20170810105439418), and the Fundamental Research Funds for the Central Universities. No formal ethical approval was required for the demonstration in Figures 2 and 4; attaching the device to the gloves was not harmful and was consented to by the volunteer.

Conflict of Interest

The authors declare no conflict of interest.

Data Availability Statement

The data that support the findings of this study are available from the corresponding author upon reasonable request.

Keywords

bimodal sensors, human–machine interaction, hydrogels, strain sensors, temperature decoupling

Received: March 14, 2023
Revised: May 15, 2023
Published online:

---

[1] a) M. Ahmad, Rafi ud, C. F. Pan, J. Zhu, *J. Phys. Chem. C* **2010**, *114*, 2560; b) M. X. Chen, C. F. Pan, T. P. Zhang, X. Y. Li, R. R. Liang, Z. L. Wang, *ACS Nano* **2016**, *10*, 6074; c) F. Li, X. D. Wang, Z. G. Xia, C. F. Pan, Q. L. Liu, *Adv. Funct. Mater.* **2017**, *27*, 8; d) F. Li, Z. G. Xia, C. F. Pan, Y. Gong, L. Gu, Q. L. Liu, J. Z. Zhang, *ACS Appl. Mater. Interfaces* **2018**, *10*, 11739; e) P. Lin, C. Pan, Z. L. Wang, *Mater. Today Nano* **2018**, *4*, 17; f) H. Liu, F. Liu, Z. Qu, J. Chen, H. Liu, Y. Tan, J. Guo, Y. Yan, S. Zhao, X. Zhao, X. Nie, X. Ma, Z. Pei, M. Liu, *Nano Res. Energy* **2023**, *2*, e9120049; g) X. Q. Liu, R. R. Liang, G. Y. Gao, C. F. Pan, C. S. Jiang, Q. Xu, J. Luo, X. M. Zou, Z. Y. Yang, L. Liao, Z. L. Wang, *Adv. Mater.* **2018**, *30*, 8; h) C. F. Pan, L. Dong, G. Zhu, S. M. Niu, R. M. Yu, Q. Yang, Y. Liu, Z. L. Wang, *Nat. Photonics* **2013**, *7*, 752; i) J. C. Sun, Y. Y. Wang, S. Q. Guo, B. S. Wan, L. Q. Dong, Y. D. Gu, C. Song, C. F. Pan, Q. H. Zhang, L. Gu, F. Pan, J. Y. Zhang, *Adv. Mater.* **2020**, *32*, 9; j) C. Wang, Y. Liu, X. C. Qu, B. J. Shi, Q. Zheng, X. B. Lin, S. Y. Chao, C. Y. Wang, J. Zhou, Y. Sun, G. S. Mao, Z. Li, *Adv. Mater.* **2022**, *34*, 11; k) Z. N. Wang, R. M. Yu, C. F. Pan, Y. Liu, Y. Ding, Z. L. Wang, *Adv. Mater.* **2015**, *27*, 1553; l) X. N. Wen, W. Z. Wu, C. F. Pan, Y. F. Hu, Q. Yang, Z. L. Wang, *Nano Energy* **2015**, *14*, 276; m) F. Zhang, X. H. Liu, C. F. Pan, J. Zhu, *Nanotechnology* **2007**, *18*, 4; n) R. R. Zhou, G. F. Hu, R. M. Yu, C. F. Pan, Z. L. Wang, *Nano Energy* **2015**, *12*, 588.
[2] a) X. Ma, C. F. Wang, R. L. Wei, J. Q. He, J. Li, X. H. Liu, F. C. Huang, S. P. Ge, J. Tao, Z. Q. Yuan, P. Chen, D. F. Peng, C. F. Pan, *ACS Nano* **2022**, *16*, 2789; b) S. Zhao, R. Zhu, *Adv. Mater. Technol.* **2017**, *2*, 9; c) S. Fu, J. Tao, W. Q. Wu, J. L. Sun, F. T. Li, J. Li, Z. H. Huo, Z. G. Xia, R. R. Bao, C. F. Pan, *Adv. Mater. Technol.* **2019**, *4*, 9; d) Q. Hua, J. Sun, H. T. Liu, R. Bao, R. Yu, J. Zhai, C. Pan, Z. L. Wang, *Nat. Commun.* **2018**, *9*, 11; e) Y. Liu, J. Tao, W. K. Yang, Y. F. Zhang, J. Li, H. L. Xie, R. R. Bao, W. C. Gao, C. F. Pan, *Small* **2022**, *18*, 11.
[3] a) G. Z. Li, S. Q. Liu, L. Q. Wang, R. Zhu, *Sci. Rob.* **2020**, *5*, 11; b) Y. Liu, R. R. Bao, J. Tao, J. Li, M. Dong, C. F. Pan, *Sci. Bull.* **2020**, *65*, 70; c) Y. M. Liu, C. K. Yiu, Z. Song, Y. Huang, K. M. Yao, T. Wong, J. K. Zhou, L. Zhao, X. C. Huang, S. K. Nejad, M. G. Wu, D. F. Li, J. H. He, X. Guo, J. S. Yu, X. Feng, Z. Q. Xie, X. G. Yu, *Sci. Adv.* **2022**, *8*, 11; d) Y. Yu, J. H. Li, S. A. Solomon, J. H. Min, J. B. Tu, W. Guo, C. H. Xu, Y. Song, W. Gao, *Sci. Rob.* **2022**, *7*, 12; e) J. He, R. H. Zhou, Y. F. Zhang, W. C. Gao, T. Chen, W. J. Mai, C. F. Pan, *Adv. Funct. Mater.* **2022**, *32*, 10.
[4] a) W. Zhang, B. Wu, S. Sun, P. Wu, *Nat. Commun.* **2021**, *12*, 12; b) Y. Dobashi, D. Yao, Y. Petel, T. N. Nguyen, M. S. Sarwar, Y. Thabet, C. L. W. Ng, E. S. Glitz, G. T. M. Nguyen, C. Plesse, F. Vidal, C. A. Michal, J. D. W. Madden, *Science* **2022**, *376*, 502; c) G.-H. Lee, H. Woo, C. Yoon, C. Yang, J. Y. Bae, W. Kim, D. H. Lee, H. Kang, S. Han, S.-K. Kang, S. Park, H.-R. Kim, J. W. Jeong, S. Park, *Adv. Mater.* **2022**, *34*, 2204159.
[5] a) J. Y. Huang, M. Zhao, Y. Hao, Q. F. Wei, *Adv. Mater. Technol.* **2022**, *7*, 14; b) Z. C. Yan, T. S. Pan, G. Yao, F. Y. Liao, Z. L. Huang, H. L. Zhang, M. Gao, Y. Zhang, Y. Lin, *Sci. Rep.* **2017**, *7*, 7; c) Y. M. Yin, Y.

L. Wang, H. Y. Li, J. Xu, C. Zhang, X. Li, J. W. Cao, H. F. Feng, G. Zhu, *Chem. Eng. J.* **2022**, *430*, 10; d) Y. Zhang, J. L. Yang, X. Y. Hou, G. Li, L. Wang, N. N. Bai, M. K. Cai, L. Y. Zhao, Y. Wang, J. M. Zhang, K. Chen, X. Wu, C. H. Yang, Y. Dai, Z. Y. Zhang, C. F. Guo, *Nat. Commun.* **2022**, *13*, 12.

[6] G. Liu, Z. Lv, S. Batool, M.-Z. Li, P. Zhao, L. Guo, Y. Wang, Y. Zhou, S.-T. Han, *Small* **2023**, 2207879.

[7] a) G. Gao, F. J. Yang, F. H. Zhou, J. He, W. Lu, P. Xiao, H. Z. Yan, C. F. Pan, T. Chen, Z. L. Wang, *Adv. Mater.* **2020**, *32*, 10; b) G. Ge, Y. Lu, X. Y. Qu, W. Zhao, Y. F. Ren, W. J. Wang, Q. Wang, W. Huang, X. C. Dong, *ACS Nano* **2020**, *14*, 218; c) G. Ge, W. Yuan, W. Zhao, Y. Lu, Y. Z. Zhang, W. J. Wang, P. Chen, W. Huang, W. L. Si, X. C. Dong, *J. Mater. Chem. A* **2019**, *7*, 5949.

[8] B. Y. Lu, H. Yuk, S. T. Lin, N. N. Jian, K. Qu, J. K. Xu, X. H. Zhao, *Nat. Commun.* **2019**, *10*, 10.

[9] Y. Lu, X. Qu, W. Zhao, Y. Ren, W. Si, W. Wang, Q. Wang, W. Huang, X. Dong, *Research* **2020**, *2020*, 2038560.

[10] a) X. Chen, R. Z. Li, G. Y. Niu, M. Y. Xin, G. Z. Xu, H. Y. Cheng, L. Yang, *Chem. Eng. J.* **2022**, *444*, 11; b) M. Saeidi-Javash, Y. P. Du, M. X. Zeng, B. C. Wyatt, B. W. Zhang, N. Kempf, B. Anasori, Y. L. Zhang, *ACS Appl. Electron. Mater.* **2021**, *3*, 2341; c) Y. Ohm, C. F. Pan, M. J. Ford, X. N. Huang, J. H. Liao, C. Majidi, *Nat. Electron.* **2021**, *4*, 313; d) H. L. Sun, Y. Zhao, S. L. Jiao, C. F. Wang, Y. P. Jia, K. Dai, G. Q. Zheng, C. T. Liu, P. B. Wan, C. Y. Shen, *Adv. Funct. Mater.* **2021**, *31*, 11.

[11] a) G. Y. Bae, J. T. Han, G. Lee, S. Lee, S. W. Kim, S. Park, J. Kwon, S. Jung, K. Cho, *Adv. Mater.* **2018**, *30*, 1803388; b) M. Cai, Z. D. Jiao, S. Nie, C. J. Wang, J. Zou, J. Z. Song, *Sci. Adv.* **2021**, *7*, 10.

[12] a) Z. L. Li, Y. Liu, X. M. Chen, H. Y. Cao, H. Y. Shen, L. Mou, X. L. Deng, X. Y. Jiang, Y. L. Cong, *Biosens. Bioelectron.* **2020**, *166*, 7; b) L. Q. Wang, R. Zhu, G. Z. Li, *ACS Appl. Mater. Interfaces* **2020**, *12*, 1953.

[13] Y. Huang, M. Zhong, Y. Huang, M. S. Zhu, Z. X. Pei, Z. F. Wang, Q. Xue, X. M. Xie, C. Y. Zhi, *Nat. Commun.* **2015**, *6*, 8.

[14] W. Cheng, X. W. Zeng, H. Z. Chen, Z. M. Li, W. F. Zeng, L. Mei, Y. L. Zhao, *ACS Nano* **2019**, *13*, 8537.

[15] D. Gan, Z. Q. Huang, X. Wang, L. L. Jiang, C. M. Wang, M. Y. Zhu, F. Z. Ren, L. M. Fang, K. F. Wang, C. M. Xie, X. Lu, *Adv. Funct. Mater.* **2020**, *30*, 10.

[16] R. G. Han, L. Wang, X. L. Tang, J. Qian, J. B. Yu, X. P. Chen, Y. X. Huang, *Mater. Lett.* **2021**, *304*, 4.

[17] J. He, P. Xiao, W. Lu, J. W. Shi, L. Zhang, Y. Liang, C. F. Pan, S. W. Kuo, T. Chen, *Nano Energy* **2019**, *59*, 422.